A 1D CNN Algorithm for Low Background β Detection with Time Projection Chamber

Zengxuan Huang, Changqing Feng* , Yuanfei Cheng, Kunjun Yang,
Songsong Tang, Zhiyong Zhang, Ruiyang Zhang, Shubin Liu

***Abstract*—Low-background β detection is crucial for environmental safety. This paper introduces a one-dimensional convolutional neural network (1D CNN) algorithm for low background β detection in Time Projection Chambers (TPC), aiming to classify β and background signals detected within the TPC detectors and recorded by the electronic system. Experimental results demonstrate the capability of the proposed algorithm in handling complex background and β signals. The neural network was processed to datasets from two different conditions, both achieved a background rejection rates of over 98%, while retaining β event rates at about 55%. Compared to traditional lead-shielded detection methods, the application of this algorithm enables lead-free, low-background β detection. This significantly reduces the instrument's size and weight, thereby greatly expanding its potential applications.**

***Index Terms*—1D Convolutional Neural Network (1D CNN), Lead-Free Shielding, Time Projection Chamber (TPC), Low Background β Detection, Charge Sensitive Amplifiers (CSA), Particle Identification.**

I. Introduction

WITH their prolonged half-lives, α and β radioactive nuclides pose health risks through ionizing radiation as they enter the human body via ecological cycles. Consequently, monitoring α and β ionizing radiation in the environment is crucial for assessing levels, identifying sources, and evaluating impacts [1]–[3]. In nuclear accident sites like Fukushima Daiichi Nuclear Power Plant, detecting α and β particles, emitted from specific nuclear fission products and plutonium in nuclear fuel, is crucial, in addition to gamma photons [4]. In common scenarios, samples with low activity levels and ambient background radiation require low-background detection methods for precise discrimination. Mainstream solutions, like multi-wire proportional chambers and scintillation detectors, are commonly employed for this purpose. [5], [6]. These methods analyze event energy to differentiate samples and background radiation. However, thick lead shielding required for low sample activity leads to bulky instruments unfit for confined spaces like nuclear power plants.

Given the aforementioned considerations, a detection scheme based on Time Projection Chambers (TPC) is introduced [7], enabling the measurement of 3D trajectories and energy deposition of charged particles [8]. By extracting and utilizing a wider array of physical features rather than solely relying on energy information, it effectively distinguishes between background signals and genuine radiation events without the need for lead shielding. In α measurement mode, this method achieves a background count rate below 1.6×10^{-3} counts per minute at a 95% confidence level, while preserving around 96% of events generated by the ^{241}Am radioactive source employed for assessing detection efficiency. However, in β mode, the similarity between various physical characteristics of background events and genuine β sources leads to a substantial reduction in the detection efficiency of β radiation when using the aforementioned algorithm for background screening.

In recent years, neural networks have been extensively incorporated into the realm of particle identification [9]–[11]. In this paper, leveraging the aforementioned lead-free shielding detection method and electronic system, a low-background β particle screening algorithm is devised using a one-dimensional CNN neural network, facilitated by waveform analysis of the samples. Applying the algorithm to experimentally derived detector data enables effective differentiation of background events while maintaining a high rate of β data retention. Additionally, by comparing detector test result before and after structural enhancements using this algorithm, the efficacy of the improvement strategies can be further validated.

II. TPC System and Waveform Characteristics

A. Detector and Readout Electronics

This algorithm is applicable to a range of TPC detection system with the capability of detecting three-dimensional trajectories and outputting waveforms. In this paper, we utilized an enhanced version of the lead-free shielding α detector previously mentioned [7] in Section I while retaining α detection capabilities, comprising both the TPC system and readout electronics.

As shown in Fig. 1, the TPC system consists of a TPC main detector with a drift length of 53 mm (referred to as TPC hereafter, while the TPC system denotes the entire system) and an anti-coincidence detector with a drift length of 8 mm assembled back-to-back. Events hitting both the TPC and anti-coincidence detectors are considered muons from cosmic rays and are thus filtered out.The readout electrodes of the TPC consist of 120 strips in both X and Y directions, each approximately 1.33 mm in width, covering a total sensitive area of 150 mm × 150 mm. The entrance aperture is circular

*Corresponding author: Changqing Feng (e-mail: fengcq@ustc.edu.cn).

This work was supported by the Fundamental Research Funds for the Central Universities (Grant No.WK2360000011).

The authors are with State Key Laboratory of Particle Detection and Electronics, University of Science and Technology of China, Hefei 230026, China.

with a diameter of 70 mm, where β particles outside this aperture are shielded by the aluminum casing of the detector. Conversely, the anti-coincidence detector comprises 16 pads, dividing the sensitive area into a 4 × 4 grid.

To validate the algorithm's applicability, tests were also conducted using an improved version of the aforementioned detector. The enhancement of the TPC comprises two key elements: externally, a drawer-shaped tray crafted from copper material is employed to house the samples, serving to mitigate a portion of the β or analogous radiation penetrating through the membrane window from the surroundings. Internally, a field cage fabricated from low-background material replaces the previous one. For convenience, the terms "Cond.A" and "Cond.A" will be used to refer to tests using these two types of detectors in the subsequent discussion. It's important to note that the PCB anode board also contributes significantly to the background. While this improvement is slated for future detector implementations, it has not yet been deployed.

Together, the readout electrodes of the two detectors constitute the 256-channel signal of the input electronic system. These signals undergo processing using a Front-End Card (FEC) [12] and a Data Collection Module (DCM) [13]. Initially, they are fed into four Application-Specific Integrated Circuits (ASICs) called ASIC for TPC Electronics (AGET) within the FEC [14], where they undergo amplifying through charge-sensitive amplifications (CSA), shaping, and sampling. Subsequently, the analog signals are digitized using four 12-bit Analog-to-Digital Converters (AD9235), after which they are packaged and uploaded to the DCM via a Xilinx Artix-7 series Field-Programmable Gate Array (FPGA). The DCM then gathers all data packets from the FEC and transmits them to a PC via Ethernet. It is worth mentioning that the algorithm discussed in this paper is not restricted to the particular detection system described above.

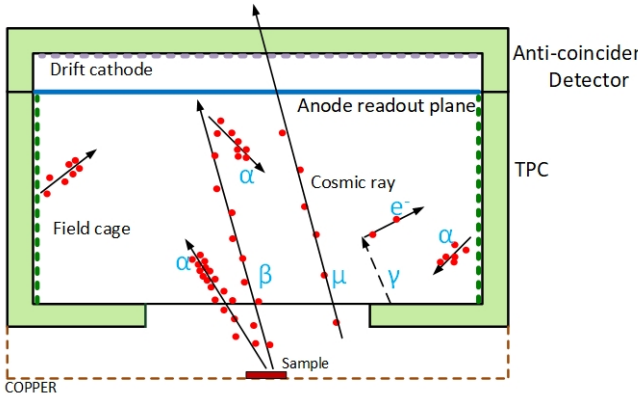

Fig. 1: Structure of the TPC system

Tests were conducted using ^{90}Sr radioactive source and empty detector without radioactive source to evaluate β and background events. Henceforth, β and background will be used to refer to these two sets of test results. The basic and the improved detector were both subjected to testing. TABLEI illustrates the total event counts of Cond.A and Cond.B These data comprise the entire dataset in Section III-C. It is evident that despite similar counting rate for the ^{90}Sr radioactive source, there is a notable decrease in the background counting rate, thus demonstrates the effectiveness of the improvements.

TABLE I: Dector Testing Result

Test Data	Events Number	Time duration	Count rate
β dataset0[1]	167,206	8min	20,900/min
β dataset1[2]	217,310	10min	21,731/min
background[2]	128,953	3h	42,984/h
background[2]	95,977	4h	23,994/h

[1] Cond.A.
[2] Cond.B.

B. Waveform Characteristics

The waveforms digitized by the electronic system mentioned in Section II-A are shown in Fig. 2, with a sampling rate of 25 MHz, a peaking time of 500 ns, and a sampling window consisting of 512 sampling points. Each event consists of several such waveforms, each representing the anode strips struck by incident particles in their respective electronic channels, while waveforms from other channels are the baseline and discarded during the upload process. These events constitute the data set of this paper.

Mapping each baseline-subtracted waveform of the aforementioned dataset to the position of the anode strips enables the reconstruction of the particle's three-dimensional trajectory and energy loss. As depicted in Fig. 2, a series of waveforms from specific events in a particular dimension enable the reconstruction of particle trajectories along that dimension within the detector, including the energy loss at each point. In addition, the reconstructed trajectory provides information on the particle's initial position and drift time in the TPC.

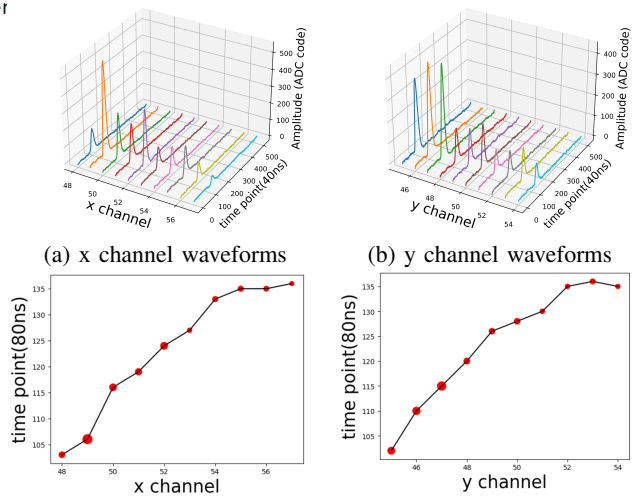

(a) x channel waveforms (b) y channel waveforms

(c) x channel trajectory and energy reconstruction (d) y channel trajectory and energy reconstruction

Fig. 2: Waveforms and trajectory energy reconstruction for individual event

III. Algorithm Design

A. Neural Network Architecture

From the preceding text, the following features of the input data can be inferred.

- Spatial structural information, implying that correlations exist not only among sampling points along the time dimension but also spatially across different waveforms.
- Translational invariance, indicating that shifting the waveforms along both the time and spatial dimensions is akin to merely altering the time and position of particle incidence, without altering other physical properties.
- Local correlation, pertaining to the interdependence among localized information in the data, such as the correspondence between the peak positions of individual waveforms and the trajectory of particles along that dimension.
- Sequential characteristics, meaning that the waveforms along the time dimension form a fixed sequence.
- Extensive characteristics, necessitating large-scale, prolonged testing datasets for training neural networks.

Based on the above reasons, a one-dimensional CNN neural network model is well-suited for this paper [15]. The algorithm proposes the following neural network structure, as shown in Fig. 3.

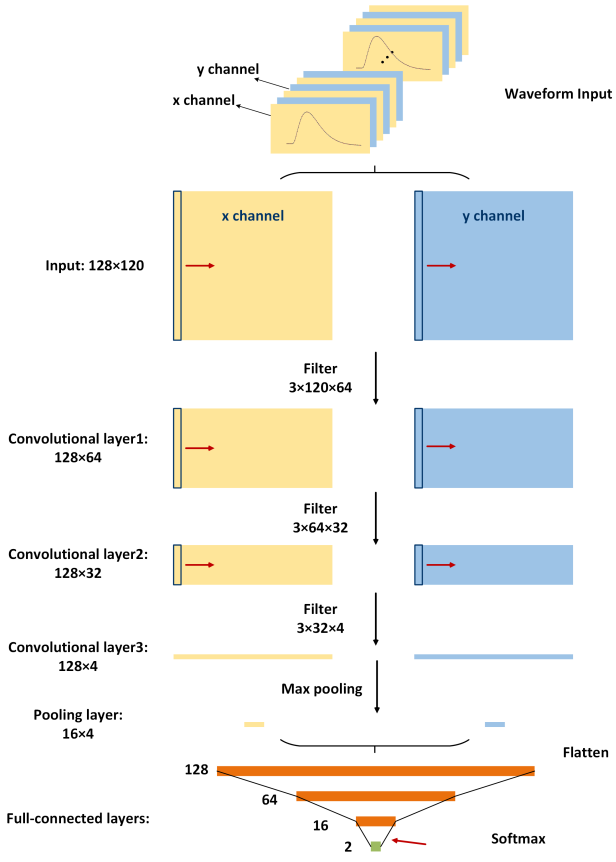

Fig. 3: Neural network architecture

The neural network comprises a dual-channel parallel one-dimensional CNN network and fully connected layers [16]. To extract waveform features from each spatial dimension, the CNN network adopts a dual-channel parallel configuration where the data from each dimension is input into its corresponding channel. In the dual-channel CNN network, each channel consists of three layers of one-dimensional convolutional layers. The basic structure of a one-dimensional convolutional layer is as follows:

$$out\left(Ni, Coutj\right) = bias\left(Coutj\right) + \sum_{k=0}^{C_{in}-1} weight\left(Coutj, k\right) \times input\left(Ni, k\right) \tag{1}$$

The terms "weight" and "bias" denote the trainable parameters encompassing the learnable weights and biases. The one-dimensional convolutional layer employs a set of learnable filters (referred to as convolutional kernels or filters) to perform convolution operations on input sequences. The network's input shape is a tensor of size 128 $\times$ 120. With 64 filters of size 3 $\times$ 120, convolution is performed over the input sequence, computing weighted summations of features within each window at every position. This process is followed by a nonlinear activation function to introduce nonlinear transformations and enhance the network's expressive power, resulting in a tensor of size 128 $\times$ 64. Subsequently, the same convolutional operation is applied with 3 $\times$ 64 $\times$32 and 3 $\times$ 64 $\times$ 4 filters sequentially. The LeakyReLU activation function is employed in the convolutional layer to address the issue of gradient vanishing often encountered with traditional activation functions like ReLU [17]. Its introduction of non-linearities to the network, as well as a group normalization operator [18] to avoid early overfitting mitigates the risk of neuron death, thus facilitating more effective updates to neurons during training.

Upon entering this channel, the data undergoes three layers of convolution before being passed through a pooling layer for output. The placement of the pooling layer after convolution is strategic, as the waveform data, representing the proportion of channels hit in each event, is relatively sparse. Directly pooling after convolution would result in significant feature loss. Hence, to enhance the extraction and preservation of diverse waveform features, convolutional layers are utilized initially for feature extraction, followed by pooling for down-sampling and feature compression. The pooling layer adopts one-dimensional max-pooling (MaxPooling1D), structured as follows:

$$out(Ni, Cj, k) = \max_{m=0,1,\ldots,kernelsize-1} input(Ni, Cj, stride \times k + m) \tag{2}$$

After the pooling layers, the data from the two channels undergo dimensionality reduction before being concatenated into a one-dimensional tensor format. This concatenated tensor is then input into a series of three fully connected layers for further feature compression and extraction.

$$y = xA^T + b \tag{3}$$

In the network's fully connected layers, the Tanh activation function is employed. This function constrains the output

within the [-1, 1] range, beneficial for scenarios needing probabilistic outputs. Furthermore, Tanh maintains gradients across the input range, aiding in gradient propagation during training and expediting convergence.

The final layer of the fully connected layers employs the sigmoid activation function. Consequently, the network generates a probability vector with two elements through the Softmax layer, indicating the likelihood of the input event being classified as either a β particle or background [19], respectively.

B. Data Preprocessing

To streamline data storage and minimize baseline interference in waveforms, the original signals were cropped from the 22nd to the 278th sampling point, followed by downsampling to yield a dataset with 128 sampling points and a sampling rate of 12.5MHz. This dataset serves as the foundation for subsequent algorithm development, as shown in Fig. 4.

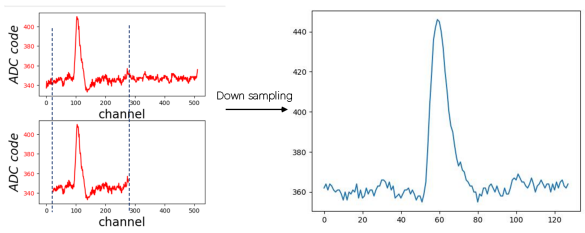

Fig. 4: Waveform truncation and downsampling

Given the constraints of computer hardware, the preprocessing of waveform data adopts sparse tensor [20] formats based on channel numbers to economize storage space further. Sparse tensors, characterized by mostly zero elements, store only the positions and values of non-zero elements. This approach optimizes the storage and processing of data in large datasets, offering increased efficiency compared to dense tensor representations. The dataset, stored in the pkl format, utilizes a sparse tensor structure on the computer's hard drive. This serialization format encodes the target data in binary form, offering superior storage efficiency and faster read/write operations compared to traditional formats like dat and csv. Particularly advantageous for managing extensive datasets, pkl ensures optimal storage utilization and computational performance.

C. Training Process

In traditional multi-event algorithms, the particle's impact position has a substantial impact on particle discrimination. To mitigate the influence of source position changes on the results, we aim for greater algorithm universality. Consequently, to simulate the real-world usage scenario of the detector and the properties of the samples a radiation source with a 1 cm radius was positioned at a distance of 5.8 cm from the detector's membrane window, ensuring a relatively uniform distribution of particle impact positions on the window. The algorithm utilizes data obtained from measurements conducted with the ^{90}Sr radioactive source, as well as background data acquired from measurements conducted without the presence of a radioactive source. Furthermore, to minimize the influence of hits occurring beyond the membrane window, we examined the distribution of hit positions for all events. Specifically, only events with hit positions within a 7 cm radius from the center were retained as training data for β events, while data outside this range were excluded ,while all background events filtered through the anti-coincidence will also be utilized in this algorithm.

The dataset, comprising background and β events, is split into training and testing sets at a 4:1 ratio. The training set is used to train the network, while the testing set evaluates the trained model's performance. During training, dynamic learning rate algorithms and Dropout layers are incorporated to enhance accuracy and prevent overfitting. Adam (adaptive moment estimation) optimization, known for its effectiveness in handling sparse gradients with minimal memory usage, is employed as the optimization algorithm during training.

The background event count rate in the dataset is low, spanning over hours, ensuring stability in the testing results over an extended period. Conversely, β events exhibit a higher count rate, covering a time span of 2 minutes every batch. For evaluating the retention rate of β events, an additional dataset from another batch was used for assessment. After training, the β event data and background event data are input into the trained network to obtain results. The network outputs a one-dimensional tensor of length 2, where each value represents the probability of the input event corresponding to a particular particle type. By applying a probability threshold, only particles with consistent labels and probabilities above the threshold are considered correctly identified as β events. This process yields the background rejection rate and particle retention rate. It's worth noting that for the background test set, which comprises 1/5 of the total number of events, assuming a stable background count rate, the corresponding time span is considered to be 1/5 of the total dataset.

During the training phase, a dynamic learning rate optimization algorithm was utilize [21]. Initially, a relatively large learning rate was applied to aid the model in converging towards local or global optima. With increasing iterations, the learning rate gradually decreased, facilitating accelerated convergence in the correct direction, rather than oscillating near the lowest gradient point. The chosen loss function for the network is the Cross Entropy Loss Function [22], which is designed based on probability distributions. It mandates that the model's output, after being transformed by the softmax function, represents a probability distribution. This encourages the model to provide accurate estimates of probabilities for different classes. Additionally, the Cross Entropy Loss Function effectively handles the weights of samples from different classes, aiding in addressing potential class imbalance issues. During network training, dropout layers [23] were integrated into the architecture. Dropout is a widely used regularization technique designed to mitigate overfitting in neural networks. It operates by randomly deactivating a fraction of neuron outputs during training, thereby diminishing interdependencies among neurons and enhancing the model's capacity for gen-

eralization.

IV. Test Results

A. Analysis of Network Outputs

The distinct structures of the detectors are likely to affect the data features to some extent. Consequently, data from both detectors were separately trained using an identical neural network architecture. The training and testing sets were sourced from distinct datasets obtained of the tests mentioned in Section II-A and Section II-B. Output distributions of basic and improved detector are depicted in Fig. 5. It's noticeable that the majority of background events are distributed closer to 0, with only a few closer to 1. This suggests that Considering the much higher β counting rate compared to the background counting rate provided in TABLEI, these distributions represent instances where the network incorrectly identifies background events as β events, and the misclassification is attributed to the presence of β or β-like events within the background instances. Conversely, for β events, there is a higher proportion of instances incorrectly classified as background, which limits the network's performance. Additionally, it's worth noting that the proportions of these misclassified β events differ between the two detectors. Using a threshold of less than 0.5 as the boundary, the proportion of misclassified β events for the basic detector is 23.25%, while for the improved detector it is 10.16%. This demonstrates the effectiveness of targeted improvements, with the latter exhibiting better performance. Importantly, instances distributed around 0.5 for both detectors can be neglected, indicating minimal instances posing challenges for the classification of the two categories. These distributions characteristics confirm the algorithm's efficacy in distinguishing between the two event types. The overlap between the two distributions is minimal. Hence, an appropriate threshold can be chosen to retain the majority of β events while eliminating almost all background events.

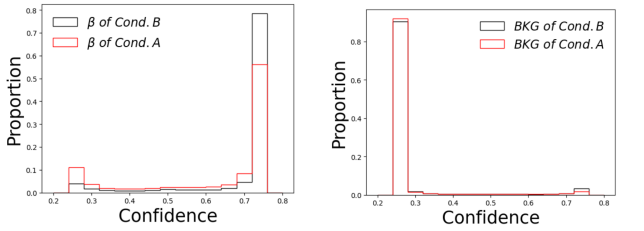

(a) Output of β events (b) Output of background events

Fig. 5: Output distribution after loading the network

B. Results of Cond.A

The test results, while maintaining β event retention above 55%, are depicted in TABLE II.

From the experimental results, it's evident that applying the algorithm to 4 minutes of β test data and randomly selecting 1/5 of the 6-hour background test data (equivalent to 1.2 hours) without additional filtering achieves a 98.34% screening rate while retaining over 55% of the β test data. This highlights the notable difference in screening effectiveness between the two scenarios, validating the algorithm's efficacy in meeting the background screening needs for low-background β detection. Moreover, the application of the algorithm to another set of β test data under identical conditions preliminarily indicates its robustness in preserving β event rates.

TABLE II: Results of Cond.A

Test Data	Events number		
	Original	***Residual***	***Rejection rate***
β dataset1[1]	85,231	46,997	44.859%
background[2]	25,791	428	98.341%

[1] 2 hour of β test data.
[2] The equivalent time is 0.6 hours.

The distribution of trajectory start points for β and background events was analyzed before and after filtering, as illustrated in Fig. 6 (missing channels are mapping onto channels with significant noise in electronic channels, so the data from those channels is discarded) . It is evident that the algorithm effectively screened events from various entry points. The reconstructed background start points distribution reveals two prominent circular patterns. The inner circle corresponds to the 7 cm diameter membrane window, while the outer circle represents the 9 cm diameter annular metal cover. The cover's thickness is smaller than that of the detector casing, resulting in a slightly higher background count outside the circle. This observation underscores the precision of the reconstructed entry positions.

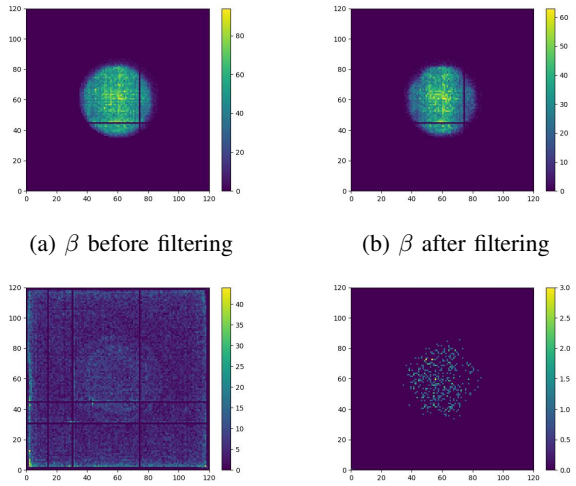

(a) β before filtering (b) β after filtering

(c) background before filtering (d) background before filtering

Fig. 6: Start points heatmap for beta and background events

The aforementioned results underscore the efficacy of the one-dimensional CNN method in background rejection. However, there's a keen interest in understanding the features of the rejected background and those retained. Consequently, post-application of the algorithm to the entire dataset, the distributions of several common physical features were analyzed, including energy loss, drift time, and trajectory lengths. Notably, for computational convenience, the Euclidean distance of vectors representing hit counts in the x and y channels was

employed to quantify trajectory lengths per event. Additionally, corresponding distributions within the initial β dataset were statistically analyzed for reference, as shown in Fig. 7, For the sake of comparability, density plots are employed to illustrate the distribution graphs.

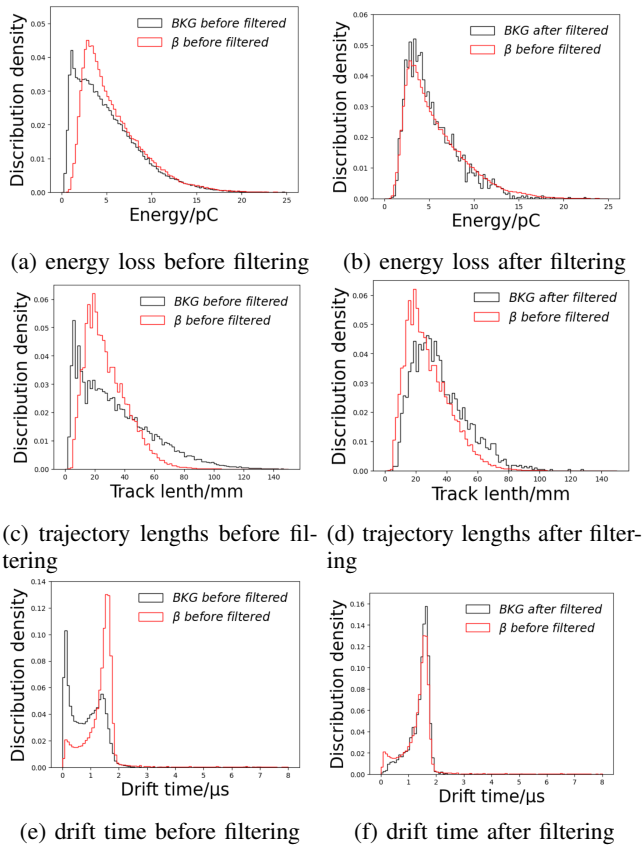

(a) energy loss before filtering (b) energy loss after filtering

(c) trajectory lengths before filtering (d) trajectory lengths after filtering

(e) drift time before filtering (f) drift time after filtering

Fig. 7: Comparison of background physical feature distributions before and after filtering with the β dataset

The test results reveal a substantial shift in the distribution of background event-related features before and after screening. Remarkably, the neural network autonomously adjusts these physical feature distributions to align more closely with those of β events, effectively screening them out. From a physical standpoint, the remaining events resemble a dataset from β source detection. This underscores the superiority of the neural network algorithm over previous methods of background rejection in lead-free shielded detection [7]: it doesn't indiscriminately discard events beyond a certain threshold based on a single feature. Instead, it employs a more nuanced comparison, resulting in the residual dataset closely mirroring the characteristics of the β dataset and achieving higher retention rates of β data, thus enhancing detection efficiency.

C. Results of Cond.B

The results after loading are as shown in TABLE III. The rejection rate of Cond.B is comparable to that of the basic detector, yet owing to the reduced number of raw background events of Cond.B within the same timeframe, a lower background count rate can be achieved, The reduction is attributed to the significant decrease in the presence of β events mixed in the background examples used for training after the TPC improvement. This further validates the effectiveness of the detector's structural improvements.

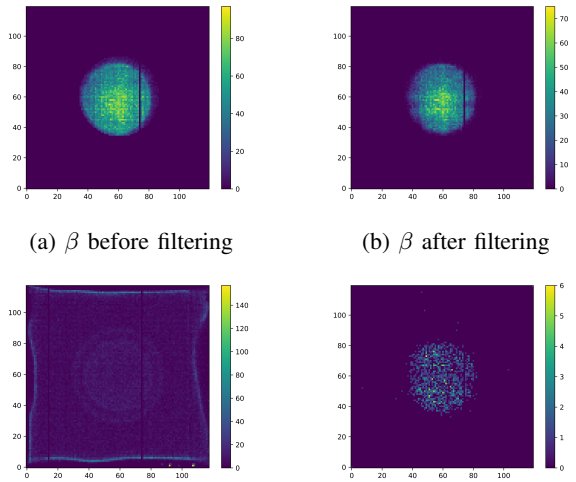

(a) β before filtering (b) β after filtering

(c) background before filtering (d) background before filtering

Fig. 8: Start heatmap points for beta and background events

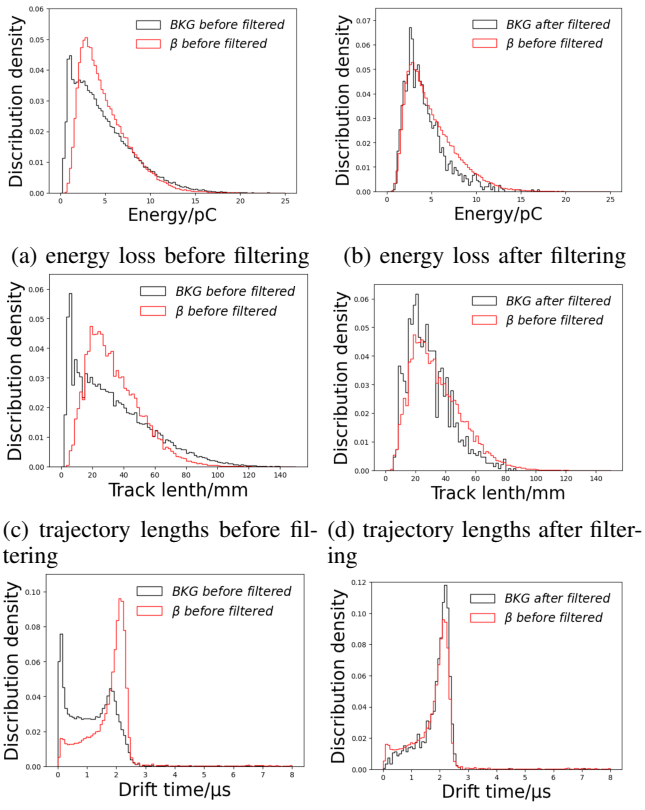

(a) energy loss before filtering (b) energy loss after filtering

(c) trajectory lengths before filtering (d) trajectory lengths after filtering

(e) drift time before filtering (f) drift time after filtering

Fig. 9: Comparison of background physical feature distributions before and after filtering with the β dataset

Based on the observed higher density of trajectory starting points within a circular membrane window of 7 cm radius

TABLE III: Results of Cond.B

Test Data	Events number		
	Original	*Residual*	*Rejection rate*
β dataset[1]	87,340	48,244	44.763%
background[2]	19,161	302	98.427%

[1] 2 hour of β test data.
[2] The equivalent time is 0.8 hours.

in the background data from basic detector, along with the comparison between the residual background physical features and those of β events, the following conclusions can be drawn: a significant portion of the background events likely stem from β particles or similar radiation, either traversing through the membrane window from the external environment or emitted from within and passing through the membrane window. The presence of β-like events mixed within the background events makes it challenging to distinguish between the two. This difficulty is evident in Fig. 5, where a considerable number of β events, when loaded into the network, are misclassified as background. Hence, improving the detection system to suppress this portion of background events can not only reduces the initial background count but also enhances the quality of the training set. The distributions of common physical quantities shown in Fig. 9, align closely with those discussed in SectionIV-B, affirming the algorithm's applicability to the improved detector.

V. Discussion

The algorithm devised in this paper is founded upon multi-parameter identification techniques [7].Through testing and result analysis, it has been demonstrated that the neural network-based background rejection algorithm developed herein achieves effective background elimination while utilizing lead-free shielding. This method offers notable advantages over traditional lead-shielded instruments, notably in reducing the weight and size of the detection system, thereby broadening its potential applications. In contrast to previous methods relying on manual selection algorithms based on multi-parameter identification, the neural network employed here extracts a more comprehensive set of features and considers a broader range of subtle factors in event rejection, rather than simply applying a single threshold for event filtering.

It's essential to acknowledge the limitations of this paper, which mainly include the following aspects:

- The dataset lacks comprehensiveness. The β data used in this paper were generated by radioactive sources placed at positions relatively distant from the membrane window. In real-world scenarios, when samples are placed in the marginal area below the membrane window, certain features such as the angle of incidence may differ from the current dataset.
- The stability of the algorithm remains to be verified and improved. Due to constraints in time and testing scenarios, the current results are inadequate to conclusively demonstrate the algorithm's stability across various environments. Therefore, the robustness of the algorithm in diverse practical application scenarios requires further investigation and enhancement.
- Further improvement is needed in the quality of the dataset. As mentioned in Section IV-A, it's apparent that the background dataset consistently includes data resembling β particles from the environment. This could potentially impact the network's performance.
- The model's utilization of the entire waveform for input significantly increases its scale, posing challenges for deployment on an FPGA, particularly for direct deployment onto the front-end acquisition board.

Based on the aforementioned limitations, the following future work needs to be undertaken:

- Enhancing the comprehensiveness of the dataset: Collecting β test data from larger-area sources or utilizing simulated data obtained from physics simulations for training purposes.
- Conducting prolonged background tests in diverse environmental conditions to enhance the quality of background data, or refining the neural network architecture, for instance, by adopting a self-supervised learning framework to mitigate the influence of background data on network performance.
- Utilizing an anode board made of low-background material further reduces the background signals generated by the detector itself.
- Reducing the input size of the network, for instance by performing feature extraction on waveform data, can facilitate practical deployment.

VI. Conclusion

This paper introduces a one-dimensional CNN-based particle identification algorithm designed for background rejection in lead-free shielded TPC detectors. Through comprehensive testing and analysis, the algorithm has proven superior to manual selection algorithms based on multi-parameter identification employed in previous studies. Consequently, it enables the utilization of more lightweight and adaptable instruments across a broader spectrum of detection scenarios. Currently, with a β event retention rate of about 55%, we have achieved a background rejection rate over 98% .

Future research efforts should concentrate on improving the dataset's quality, exploring advanced network architectures, and conducting extensive long-term testing. These endeavors will further enhance the network's performance and robustness.

References

[1] N. R. Council, D. on Earth, L. Studies, C. on Life Sciences, and C. on the Biological Effects of Ionizing Radiations, "Health risks of radon and other internally deposited alpha-emitters: Beir iv," 1988.

[2] S. Sarvajayakesavalu, D. Lakshminarayanan, J. George, S. Magesh, K. Anilkumar, G. Brammanandhan, A. Chandrasekara, and M. Ravikumar, "Geographic information system mapping of gross alpha/beta activity concentrations in ground water samples from karnataka, india: A preliminary study," *Groundwater for sustainable development*, vol. 6, pp. 164–168, 2018.

[3] F. Edition, "Guidelines for drinking-water quality," *WHO chronicle*, vol. 38, no. 4, pp. 104–8, 2011.

[4] S. Yamamoto and J. Hatazawa, "Development of an alpha/beta/gamma detector for radiation monitoring," *Review of Scientific Instruments*, vol. 82, no. 1, p. 113503, 11 2011. [Online]. Available: https://doi.org/10.1063/1.3658821

[5] W. Warburton and B. Dwyer-McNally, "Electronic background rejection in a new ultra-low background alpha-particle counter," *Nuclear Instruments and Methods in Physics Research Section B: Beam Interactions with Materials and Atoms*, vol. 263, no. 2, pp. 221–224, 2007, industrial Radiation and Radioisotope Measurement Applications.

[6] Y. Morishita, A. Di Fulvio, S. Clarke, K. Kearfott, and S. Pozzi, "Organic scintillator-based alpha/beta detector for radiological decontamination," *Nuclear Instruments and Methods in Physics Research Section A: Accelerators, Spectrometers, Detectors and Associated Equipment*, vol. 935, pp. 207–213, 2019.

[7] J. Pan, Z. Zhang, C. Feng, D. Wang, R. Zhang, and S. Liu, "An ultra-low background alpha detection system with a micromegas-based time projection chamber," *Review of Scientific Instruments*, vol. 93, no. 1, 2022.

[8] D. R. Nygren, "Proposal to investigate the feasibility of a novel concept in particle detection," *LBL internal report*, 1974.

[9] P. Abratenko, M. Alrashed, R. An, J. Anthony, J. Asaadi, A. Ashkenazi, S. Balasubramanian, B. Baller, C. Barnes, G. Barr *et al.*, "Convolutional neural network for multiple particle identification in the microboone liquid argon time projection chamber," *Physical Review D*, vol. 103, no. 9, p. 092003, 2021.

[10] R. Sinkus and T. Voss, "Particle identification with neural networks using a rotational invariant moment representation," *Nuclear Instruments and Methods in Physics Research Section A: Accelerators, Spectrometers, Detectors and Associated Equipment*, vol. 391, no. 2, pp. 360–368, 1997.

[11] C. Adams, M. Alrashed, R. An, J. Anthony, J. Asaadi, A. Ashkenazi, M. Auger, S. Balasubramanian, B. Baller, C. Barnes *et al.*, "Deep neural network for pixel-level electromagnetic particle identification in the microboone liquid argon time projection chamber," *Physical Review D*, vol. 99, no. 9, p. 092001, 2019.

[12] D. Zhu, S. Liu, C. Feng, C. Li, J. Dong, H. Chen, Z. Chen, and J. Pan, "Development of the front-end electronics for pandax-iii prototype tpc," *IEEE Transactions on Nuclear Science*, vol. 66, no. 7, pp. 1123–1129, 2019.

[13] C. Li, C. Feng, D. Zhu, S. Liu, and Q. An, "An optical fiber-based flexible readout system for micro-pattern gas detectors," *Journal of Instrumentation*, vol. 13, no. 04, p. P04013, 2018.

[14] D. Calvet, "A versatile readout system for small to medium scale gaseous and silicon detectors," *IEEE Transactions on Nuclear Science*, vol. 61, no. 1, pp. 675–682, 2014.

[15] S. Kiranyaz, O. Avci, O. Abdeljaber, T. Ince, M. Gabbouj, and D. J. Inman, "1d convolutional neural networks and applications: A survey," *Mechanical systems and signal processing*, vol. 151, p. 107398, 2021.

[16] C. Adams, M. Del Tutto, J. Asaadi, M. Bernstein, E. Church, R. Guenette, J. M. Rojas, H. Sullivan, and A. Tripathi, "Enhancing neutrino event reconstruction with pixel-based 3d readout for liquid argon time projection chambers," *Journal of Instrumentation*, vol. 15, no. 04, p. P04009, 2020.

[17] J. Xu, Z. Li, B. Du, M. Zhang, and J. Liu, "Reluplex made more practical: Leaky relu," in *2020 IEEE Symposium on Computers and communications (ISCC)*. IEEE, 2020, pp. 1–7.

[18] Y. Wu and K. He, "Group normalization," in *Proceedings of the European conference on computer vision (ECCV)*, 2018, pp. 3–19.

[19] Y. Liao, W. Wang, Z. Zhang, S. Zhao, Y. Niu, and X. Liu, "A novel method based on adaptive autoencoder and improved long short-term memory and gated recurrent unit for nuclear radiation measurement and monitoring," *Measurement*, vol. 199, p. 111571, 2022.

[20] "torch.sparse 2014; PyTorch 2.2 documentation — pytorch.org," https://pytorch.org/docs/stable/sparse.html, [Accessed 29-03-2024].

[21] P. Baldi and P. J. Sadowski, "Understanding dropout," *Advances in neural information processing systems*, vol. 26, 2013.

[22] Z. Zhang and M. Sabuncu, "Generalized cross entropy loss for training deep neural networks with noisy labels," *Advances in neural information processing systems*, vol. 31, 2018.

[23] "Dropout 2014; PyTorch 2.2 documentation — pytorch.org," https://pytorch.org/docs/stable/generated/torch.nn.Dropout.html, [Accessed 31-03-2024].